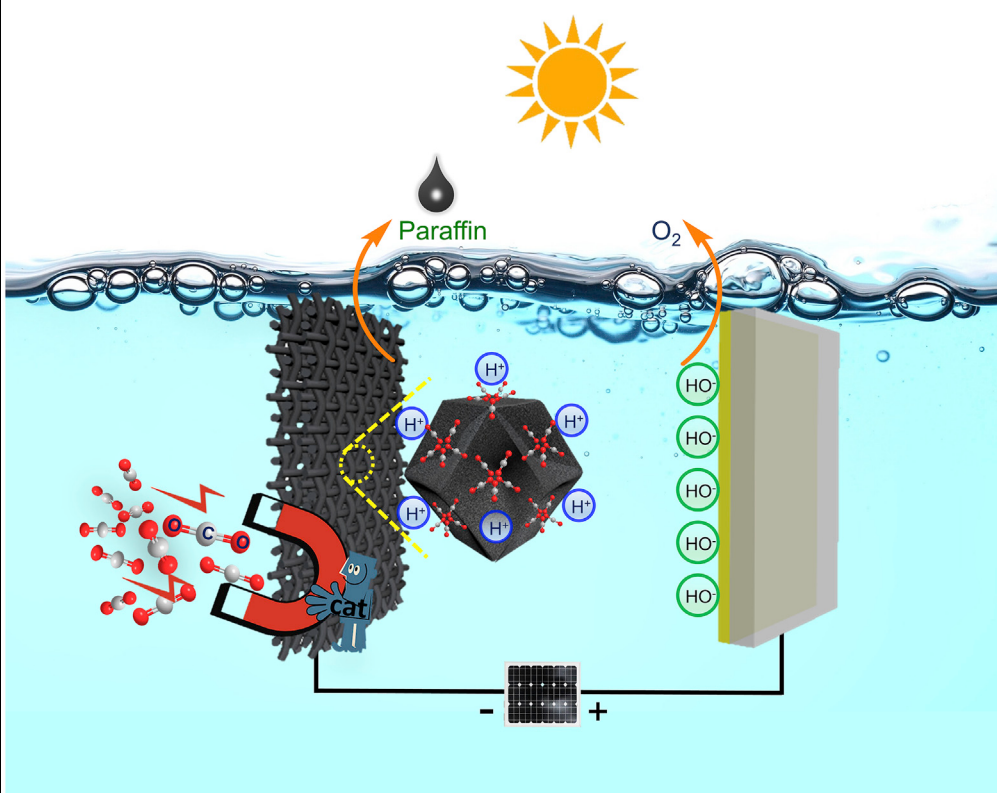
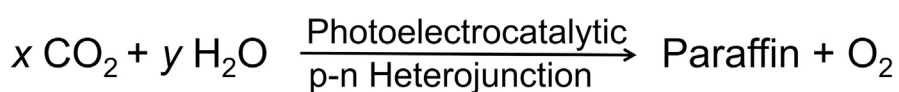


Article

Photoelectrocatalytic Reduction of CO₂ to Paraffin Using p-n Heterojunctions

Jinyuan Wang,
Yongji Guan,
Xiaogang Yu, ...,
Yilin Wang, Bin
Hu, Huanwang
Jing

hwjing@lzu.edu.cn

HIGHLIGHTS

Heterojunctions of Zn_x:Co_y@Cu are applied in photoelectrocatalytic reduction of CO₂

Multiple active sites result in excellent C-C coupling like natural photosynthesis

Photoelectrocatalytic system can tolerate the higher voltage without H₂ emission

Paraffin product is reported for the first time in CO₂ reduction

Wang et al., iScience 23, 100768
January 24, 2020 © 2019 The Author(s).
<https://doi.org/10.1016/j.isci.2019.100768>



Article

Photoelectrocatalytic Reduction of CO₂ to Paraffin Using p-n Heterojunctions

Jinyuan Wang,¹ Yongji Guan,¹ Xiaogang Yu,¹ Youzhi Cao,¹ Jiazang Chen,² Yilin Wang,³ Bin Hu,⁴ and Huanwang Jing^{1,2,5,*}

SUMMARY

Nowadays, photoelectrocatalytic (PEC) reduction of CO₂ represents a very promising solution for storing solar energy in value-added chemicals, but so far it has been hampered by the lack of highly efficient catalyst of photocathode. Enlightened by the Calvin cycle of plants, here we show that a series of three-dimensional C/N-doped heterojunctions of Zn_x:Co_y@Cu are successfully fabricated and applied as photocathodes in the PEC reduction of CO₂ to generate paraffin product. These materials integrate semiconductors of p-type Co₃O₄ and n-type ZnO on Cu foam to construct fine heterojunctions with multiple active sites, which result in excellent C-C coupling control in reduction of CO₂. The best catalyst of Zn_{0.2}:Co₁@Cu yields paraffin at a rate of 325 µg·h⁻¹ under -0.4 V versus saturated calomel electrode without H₂ release. The apparent quantum efficiency of PEC cell is up to 1.95%.

INTRODUCTION

Solar energy as a clean, cheap, and sustainable energy source remains the final hope to human beings. Photosynthesis in plants and algae can efficiently utilize sunlight to convert CO₂ and water to various organic compounds and O₂ that feed organisms to complete the natural carbon cycle in the planet (Govindjee and Krogmann, 2004; Nürnberg et al., 2018). The photoelectrocatalytic (PEC) reduction of CO₂ can be termed as *artificial photosynthesis*, which mimics natural photosynthesis and efficiently converts CO₂ and H₂O into hydrocarbons and O₂, tackling both energy and global environmental problems (Halmann, 1978; Wang et al., 2019). Recently, semiconductors are commonly utilized as catalysts in PEC reduction of CO₂, because they combine the advantages of both photocatalysis and electrocatalysis (EC) to promote the separation of photogenerated electron-holes leading to high solar conversion efficiency (Chang et al., 2019). However, their product distribution is usually limited to C1 and C2 compounds (CO, HCOOH, CH₃OH, and C₂H₅OH, etc.) (Barton et al., 2008; Cardoso et al., 2018; Schreier et al., 2015; Shan et al., 2019). In contrast, the production of multi-carbon chemicals is much sought after as potential sustainable fuels, which represents a promising path toward establishing a carbon-neutral cycle (Loiudice et al., 2016; Zhuang et al., 2018). Unfortunately, it is difficult to generate multi-carbon chemicals using direct CO₂ reduction owing to the low activity of the present catalysts in C-C coupling. This is currently the major scientific challenge in sustainable energy research.

Based on the knowledge of Calvin cycle (Bassham et al., 1954; Mao et al., 2004), we speculate that the photocathode of three-dimensional (3D) semiconductor heterojunction with multiple active sites is favorable for C-C coupling process in CO₂ reduction. Recently, our groups introduced that constructing suitable semiconductor heterojunctions is a valuable strategy to improve their PEC performances (Xu et al., 2018) by enhancing the efficiency of separation of photogenerated electron-holes. Moreover, nitrogen-modified semiconductors show favorable performance in the absorption and activation of CO₂ (Jia et al., 2017). In addition, metal oxides have been explored as efficient PEC catalysts. Among them, Co₃O₄ is an important p-type semiconductor with attractive photoelectric properties (Long et al., 2006; Tang et al., 2016); ZnO has been recognized as an excellent material for photocatalytic reactions (Liu et al., 2016; Yu et al., 2015), and Cu is confirmed in previous work as a unique metal that retains the significant faradaic yields of hydrocarbons and oxygenates (Lee et al., 2018; Lum and Ager, 2018; Shibata et al., 2008). As mentioned above, we choose Zn/Co-based zeolitic imidazolate frameworks (Zn_x:Co_y-ZIFs) as the substrates that were *in situ* assembled on Cu foam and led to Zn_x:Co_y@Cu through a calcined process.

Herein, we report that well-designed 3D C/N-doped heterojunctions of Zn_x:Co_y@Cu *in situ* integrated semiconductors of p-type Co₃O₄ with n-type ZnO on Cu foam are successfully used as photocathode in PEC cell for efficient solar-driven CO₂ reduction. Notably, visible paraffin is produced through excellent

¹State Key Laboratory of Applied Organic Chemistry, College of Chemistry and Chemical Engineering, Lanzhou University, Lanzhou 730000, China

²State Key Laboratory of Coal Conversion, Institute of Coal Chemistry, Chinese Academy of Sciences, Taiyuan 030001, China

³Key Laboratory of Colloid, Interface and Chemical Thermodynamics, Chinese Academy of Sciences, Beijing 100190, China

⁴State Key Laboratory for Oxo Synthesis and Selective Oxidation, Lanzhou Institute of Chemical Physics, Chinese Academy of Sciences, Lanzhou 730000, China

⁵Lead Contact

*Correspondence:
hwjing@lzu.edu.cn

<https://doi.org/10.1016/j.isci.2019.100768>



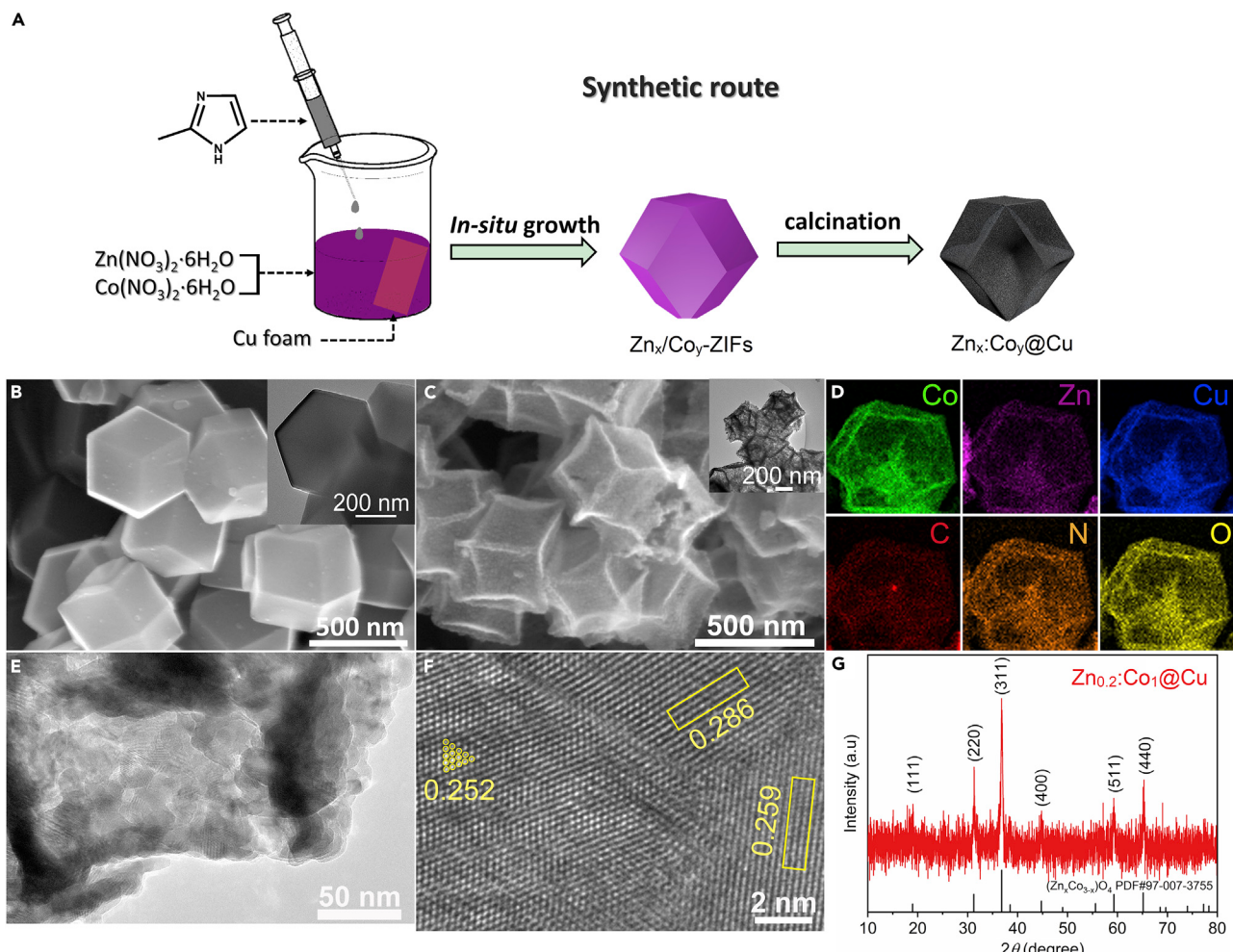


Figure 1. The Structure Characterization of $Zn_{0.2}:Co_1@Cu$

(A) Schematic illustration of the fabrication procedures of $Zn_x:Co_y@Cu$ photocathode.

(B) SEM images of $Zn_{0.2}:Co_1$ -ZIFs.

(C) SEM images of $Zn_{0.2}:Co_1@Cu$. See also Figure S1.

(D) Elemental mapping images of $Zn_{0.2}:Co_1@Cu$.

(E) TEM image of $Zn_{0.2}:Co_1@Cu$.

(F) HRTEM image of $Zn_{0.2}:Co_1@Cu$. See also Figure S4.

(G) Corresponding X-ray diffraction patterns. See also Figures S2 and S3.

C-C coupling control in our PEC cell of $Zn_x:Co_y@Cu$ | $KHCO_3$ | $BiVO_4$. We reason that the possible mechanism of generating paraffin product arises from these ideal heterojunctions that ameliorate their abilities of harvesting solar light and enhance the separation efficiency of photogenerated electron-holes; the multiple active sites of catalyst result in a cooperative effect to realize high efficiency of C-C coupling and suppress H_2 release. This is an important scientific discovery because this is the first tangible evidence uncovering chain propagation during PEC reduction of CO_2 over semiconductor photocathode.

RESULTS AND DISCUSSION

Preparation and Characterizations of Photocathodes

The fabrication procedures of $Zn_x:Co_y@Cu$ are illustrated in Figure 1A, and the experimental details are summarized in the *Transparent Methods*. The precursors of Zn_x/Co_y -ZIFs are synthesized based on reported method (Banerjee et al., 2008; Wu et al., 2014); their morphology shows a regular dodecahedron structure (Figure 1B). In this work, the samples are prepared with different molar ratios of $Zn(NO_3)_2 \cdot 6H_2O$

to $\text{Co}(\text{NO}_3)_2 \cdot 6\text{H}_2\text{O}$, and the actual ratios are determined by inductively coupled plasma-optical emission spectroscopy and listed in [Table S1](#). We take the $\text{Zn}_{0.2}\text{:Co}_1@\text{Cu}$ photocathode as the model catalyst for analyzing the morphology and structure. Scanning electron microscopy reveals an approximate diameter of 400-nm shrink hollow dodecahedron structure with sharp edges and rough surfaces ([Figure 1C](#) and [Table S2](#)). The X-ray diffraction patterns demonstrate spinel structure for $\text{Zn}_x\text{Co}_{3-x}\text{O}_4$ ([Figure 1G](#)). High-resolution transmission electron microscopic (HRTEM) analysis indicates that the clear lattice fringes are related to the plane (220) of Co_3O_4 (2.86 Å), the plane (002) of ZnO (2.59 Å), and the plane (002) of CuO (2.52 Å) ([Figure 1F](#)). In addition, the rough surfaces of $\text{Zn}_{0.2}\text{:Co}_1@\text{Cu}$ reveal abundant defects ([Figure 1E](#)), which are composed of missing link/cluster in crystal as well as residues of N for replacing O in metal oxide phases ([Liu et al., 2019](#)). The elemental mapping ([Figure 1D](#)) images illustrate that the Zn, Co, Cu, C, N, and O elements are uniformly distributed in the dodecahedral structure of $\text{Zn}_{0.2}\text{:Co}_1@\text{Cu}$, in which Cu is doped in dodecahedron due to the dissolution of a fraction of Cu foam. Thus multiple active sites would be composed of multicomponent metal and defects and activate CO_2 molecules in reaction. [Figures S1–S4](#) summarize the morphology and structures of heterojunctions $\text{Zn}_x\text{:Co}_y@\text{Cu}$, which confirm that various molar ratios of Zn to Co give rise to different crystal phases: $\text{Zn}_0\text{:Co}_1@\text{Cu}$ to cubic Co_3O_4 , $\text{Zn}_1\text{:Co}_1@\text{Cu}$ to hexagonal ZnO , and cubic Co_3O_4 , $\text{Zn}_1\text{:Co}_0@\text{Cu}$ to hexagonal ZnO .

PEC Performance of Photocathodes

The photocurrent densities of representative four photocathodes show excellent characteristic curves of photoelectron response ([Figure 2A](#)), in which photocathode of $\text{Zn}_{0.2}\text{:Co}_1@\text{Cu}$ gives the highest photocurrent. The linear sweep voltammetry curves ([Figure 2B](#)) show that the current density under PEC condition is much higher than that under argon and EC condition. Furthermore, the cyclic voltammetry curves demonstrate that the CO_2 reduction peak of photocathode $\text{Zn}_{0.2}\text{:Co}_1@\text{Cu}$ is approximately at -0.4 V versus saturated calomel electrode (SCE) ([Figure S5](#)).

We investigate the performance of CO_2 reduction by using PEC cells of $\text{Zn}_x\text{:Co}_y@\text{Cu} | \text{KHCO}_3 | \text{BiVO}_4$. Under potential of -0.4 V versus SCE, liquid products such as methanol (MeOH), ethanol (EtOH), and acetone can be detected in almost all PEC cells ([Figure S13](#)). The PEC cell of $\text{Zn}_{0.2}\text{:Co}_1@\text{Cu} | \text{KHCO}_3 | \text{BiVO}_4$ gains the topmost yield of paraffin at a rate of $325 \mu\text{g h}^{-1}$ and releases O_2 at a rate of $41 \mu\text{mol h}^{-1}$ ([Figure 2C](#)). The apparent quantum efficiency value of $\text{Zn}_{0.2}\text{:Co}_1@\text{Cu}$ reaches 1.95%, which is about 9 times larger than that of the $\text{Zn}_0\text{:Co}_1@\text{Cu}$ if its apparent faradaic efficiency equals 100% ([Figure 2D](#)). In addition, we test the activity of catalyst $\text{Zn}_{0.2}\text{:Co}_1@\text{Cu}$ under different potentials from -0.2 to -1.3 V versus SCE ([Figure S6](#)). The paraffin products are generated under all potentials due to good C-C coupling control. Notably, this type of PEC system can tolerate voltages of up to -3.3 V (-1.0 versus SCE) to yield paraffin and release O_2 at a rate of $181 \mu\text{mol h}^{-1}$ without H_2 emission ([Figure S7](#) and [Video S1](#)), which has possible potential application in industry.

To further understand the behavior of this effective PEC cell, its electrochemical impedance spectroscopy is obtained under EC condition ([Figure 2E](#)). The second arc radius of $\text{Zn}_{0.2}\text{:Co}_1@\text{Cu}$ is smaller than others, which suggests a faster interfacial charge transfer from the cathode to electrolyte and favors the formation of active hydrogen atoms reducing CO_2 to paraffin. Besides, Mott-Schottky (M-S) relationships of $\text{Zn}_x\text{:Co}_y@\text{Cu}$ are gained to illustrate their semiconductor properties and carrier concentration (N_q) ([Figures 2F](#) and [S9](#)). The slopes of the M-S curves present both positive and negative values for the $\text{Zn}_x\text{:Co}_y@\text{Cu}$ cathode, implying the successful formation of p-n heterojunction of n-type ZnO and p-type Co_3O_4 on Cu foam ([Cardon and Gomes, 1978](#)). Furthermore, the N_q values of all cathodes can be calculated by the slopes of M-S curves, in which a lower slope of M-S curve reflects a higher N_q ([Luo et al., 2013](#)). Therefore, the N_q of the $\text{Zn}_{0.2}\text{:Co}_1@\text{Cu}$ is higher than that of others ([Figure S9D](#)); this is the main reason why $\text{Zn}_{0.2}\text{:Co}_1@\text{Cu}$ shows high photocurrent. Theoretically, the inner electric field will be built in the interfaces of p-n heterojunctions ([Zhang et al., 2010](#)). Specifically, charge carriers inside the $\text{Zn}_x\text{:Co}_y@\text{Cu}$ are diffused and drifted between p-type Co_3O_4 (2.76 eV) and n-type ZnO (3.24 eV) ([Mohamed Reda et al., 2017; Tak and Yong, 2008](#)), thus forming a depletion layer at the interface. In this depletion layer a built-in electric field is formed due to the formation of positive and negative charges at the n- and p-sides, respectively. When the p-n heterojunction of $\text{Zn}_x\text{:Co}_y@\text{Cu}$ is irradiated, it can enhance the concentration of carriers and tolerance for high external voltage, resulting in high efficiency of photogenerated electron-hole separation and excellent performance in CO_2 reduction. UV-visible absorption spectra of $\text{Zn}_x\text{:Co}_y@\text{Cu}$ catalysts reveal good absorption near UV to visible light (300–1,000 nm) ([Figure S10](#)). Therefore the heterojunctions not only ameliorate the ability of harvesting solar light but also obviously enhance the separation efficiency of photogenerated electron-holes.

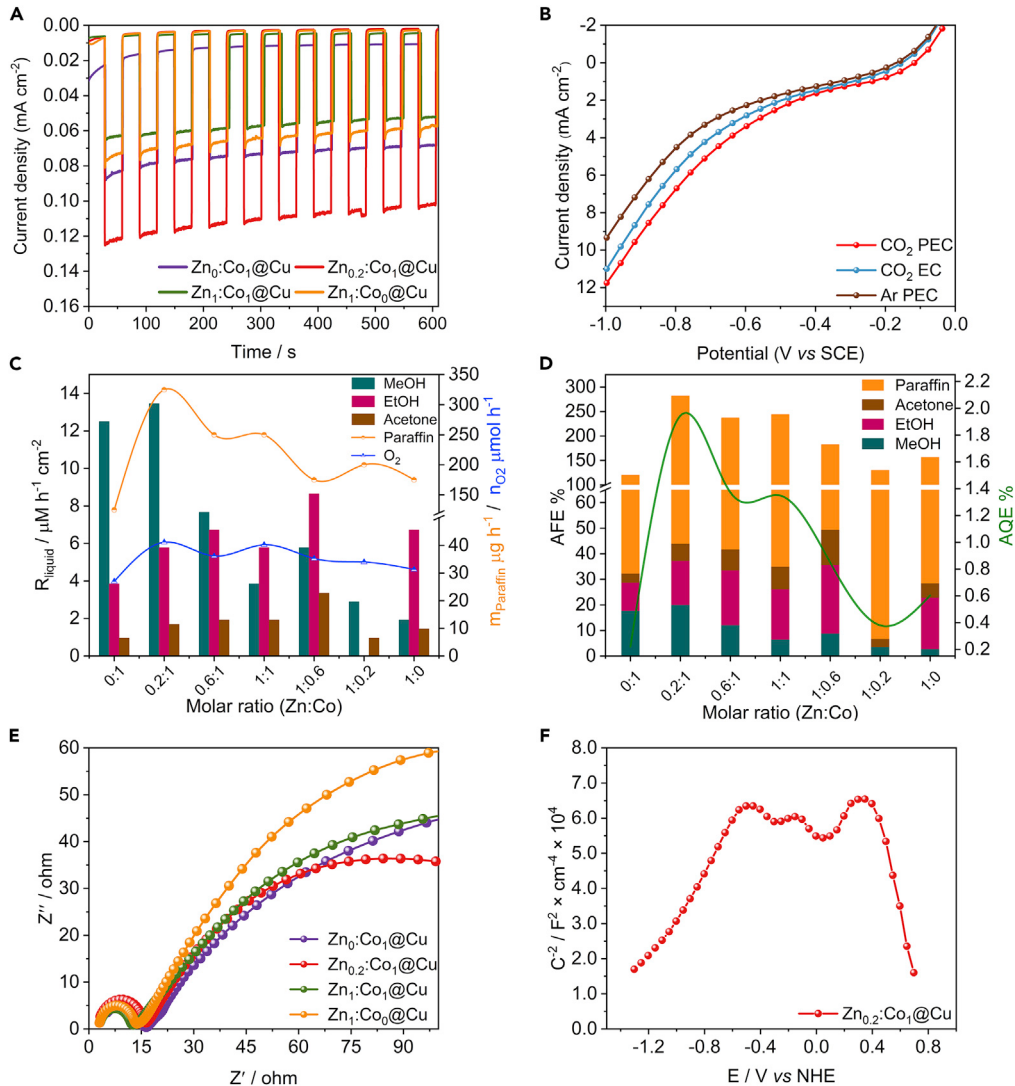
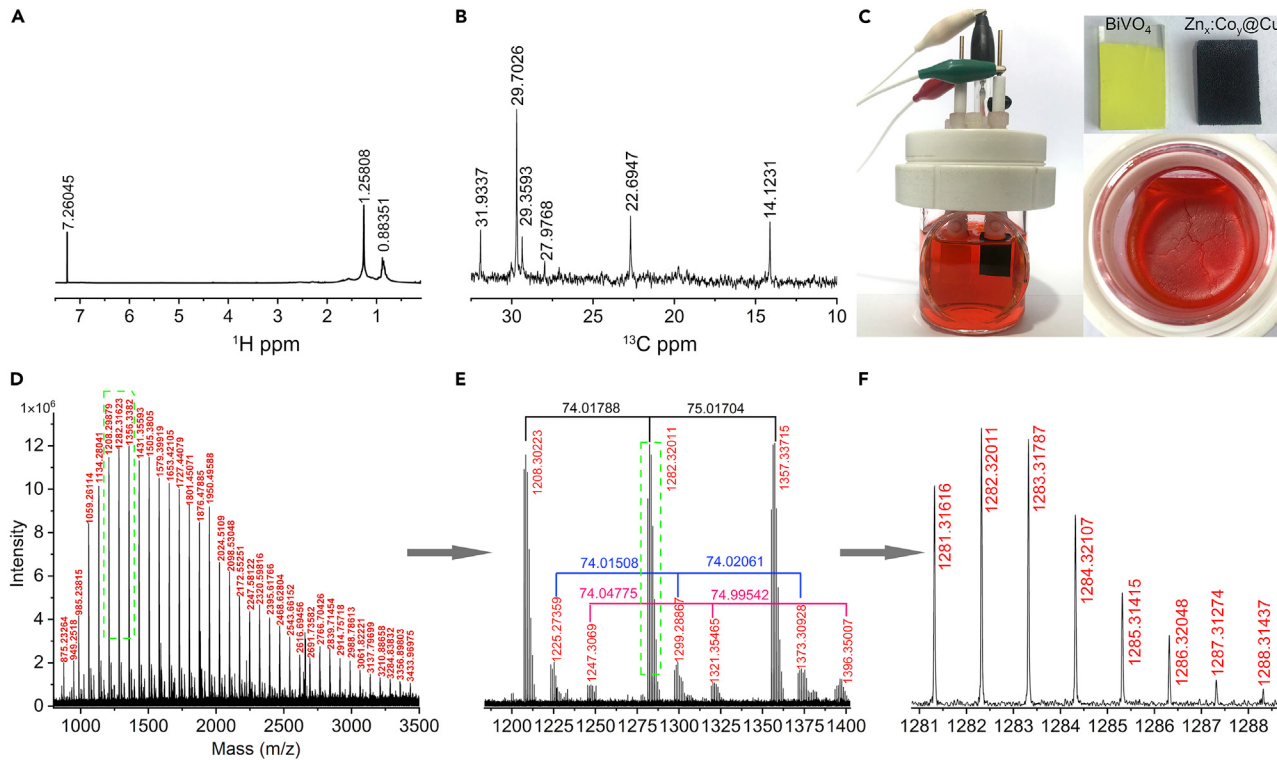


Figure 2. Catalytic Performances of $\text{Zn}_x:\text{Co}_y@\text{Cu}$ in PEC Cell

- (A) Photocurrent densities as a function of $\text{Zn}_x:\text{Co}_y@\text{Cu}$ at -1 V in the two-electrode system.
- (B) Linear sweep voltammetry curves of $\text{Zn}_{0.2}:\text{Co}_1@\text{Cu}$ electrodes under EC and PEC conditions. See also Figure S8.
- (C) The evolution rate of hydrocarbon and O_2 under the different molar ratio of Zn to Co photocathodes at -0.4 V versus SCE. See also Video S1.
- (D) Apparent faradaic efficiency (AFE) and apparent quantum efficiency (AQE) of PEC cells.
- (E) Nyquist plots of different photocathodes.
- (F) M-S plot of $\text{Zn}_{0.2}:\text{Co}_1@\text{Cu}$ photocathode. See also Figure S9.

Paraffin Product Characterization

To clarify the structure of paraffin product (Figure 3C), the ^1H NMR, ^{13}C NMR, and infrared spectra (Figures 3A, 3B, and S11B) are obtained. The typical peaks confirm a mixture of long-chain alkane compounds. The corresponding visible paraffin product is shown in Figure 3B; when the electrolyte was standing for several days, the transparent visible paraffin-like product floated on the surface of electrolyte (Figure S12). To trace the carbon source, $^{13}\text{CO}_2$ labeling experiments are also carried out by using $\text{Zn}_{0.2}:\text{Co}_1@\text{Cu}$ as photocathode. The distribution of molecular weight of the ^{13}C labeling products is carefully examined by matrix-assisted laser desorption ionization time-of-flight mass spectrometry (MALDI-TOF MS). We can find that these paraffin products are a series of long-chain oxygen-containing hydrocarbons and their molecular weight increases from 875 to 3,434 (Figure 3D). As shown in Figure 3E, we speculate that these paraffin products might have the following structural formula: $[^{13}\text{CH}_2\text{OH}(^{13}\text{CH}_2)_{55}(\text{CH}_2)_7][(^{13}\text{CH}_2)_4(\text{CH}_2)_3]\text{CH}_2\text{OH}$ for 1208; $[^{13}\text{CH}_2\text{OH}(^{13}\text{CH}_2)_{54}(\text{CH}_2)_7][(^{13}\text{CH}_2)_4(\text{CH}_2)_3]$

**Figure 3. Paraffin Detection**

Paraffin is obtained through 4-h reaction under -0.4 V versus SCE using photocathode of $\text{Zn}_{0.2}:\text{Co}_1@\text{Cu}$.

(A) ^1H NMR spectrum of paraffin in CDCl_3 .

(B) Corresponding ^{13}C NMR.

(C) PEC cell, photoelectrodes, and paraffin floated onto the electrolyte after reaction. See also Figure S12.

(D) Complete MALDI-TOF MS spectra of ^{13}C -paraffin.

(E) Unit of C5 (74, 75 mass).

(F) The isotopic distribution of ^{13}C species. See also Figure S11.

$[^{13}\text{CHOH}] \text{CH}_2\text{OH}$ for 1225, and $[^{13}\text{CH}_2\text{OH}(^{13}\text{CH}_2)_{54}(\text{CH}_2)][^{13}\text{CH}_2]_{20} (\text{CHOH})_2 \text{CH}_2\text{OH}$ for 1247. Therefore, we can see that the long chain grows step by step with a unit of C5 (74 ($^{13}\text{CH}_2)_4(\text{CH}_2)$ or 75 ($^{13}\text{CH}_2)_5$), which is like a unit of C6 glucose in the Calvin cycle of plant cell. Obviously, Figure 3F further illustrates that the peak with a molecular weight of 1,283 in the case of using $^{13}\text{CO}_2$ as the carbon source is very strong; this means the PEC cell converts CO_2 and H_2O to paraffin products. The common experiment of CO_2 reduction in PEC cell of $\text{Zn}_{0.2}:\text{Co}_1@\text{Cu}/\text{KHCO}_3/\text{BiVO}_4$ gives similar long-carbon-chain compounds: $[\text{CH}_3(\text{CH}_2)_{51}\text{CH}_2\text{OH}][(\text{CH}_2)_{20}]_x$ (1039, 1320, 1601, 1882, $x = 1, 2, 3, 4$) and $[\text{CH}_2\text{OH}(\text{CH}_2)_{80}\text{CH}_2\text{OH}]$ for 1183 (Figure S11A). These phenomena could be attributed to the proper 3D dodecahedra structure of heterojunction with multiple active sites favoring C-C coupling. The $\text{C}_{54}\text{H}_{110}$ (801) long-chain hydrocarbon is a basic unit that could be generated by the control of dodecahedral cage and multiple active sites for C-C coupling.

Structure Analyses via X-Ray Absorption Fine Structure Spectroscopy about $\text{Zn}_{0.2}:\text{Co}_1@\text{Cu}$

For a deeper understanding of the relationship between the activity and the structural feature of catalysts, the fine valence states of Co, Zn, and Cu are revealed by X-ray absorption edge structure analyses. The Co K-edge X-ray absorption near-edge structure (XANES) spectra of $\text{Zn}_x:\text{Co}_y@\text{Cu}$ exhibit similar features, indicating that Co_3O_4 phase is formed in each sample (Figure 4A). In detail, the illustration II in Figure 4A shows that the average valence state of Co elements in $\text{Zn}_{0.2}:\text{Co}_1@\text{Cu}$ is higher than that in others. The octahedral coordination has a lower intensity at peak I than the tetrahedron one, as well as a higher intensity at peak III in Figure 4A. These imply that some Co^{2+} cations in the lattice of crystal Co_3O_4 are replaced by Zn^{2+} cations (Rong et al., 2015) (Figure S14). The Zn K-edge XANES spectrum of $\text{Zn}_{0.2}:\text{Co}_1@\text{Cu}$ appears as an absorption edge energy at 9,668.9 eV that is typical characteristics of Zn^{2+} . The two small shoulders at 9,664.8 and 9,674.4 eV indicate that some tetrahedra of Zn-N are successfully retained in this catalyst compared with

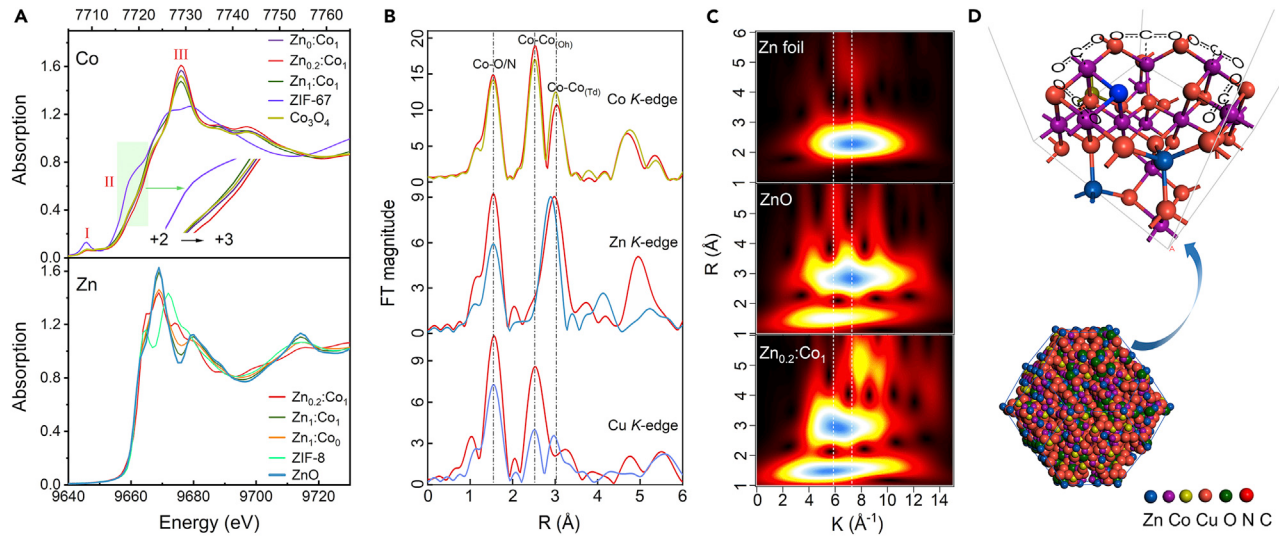


Figure 4. Results of XAFS Spectroscopy and Depicted Structures for Zn_{0.2}:Co₁@Cu

(A) The XANES spectra of Co and Zn for Zn_x:Co_y@Cu with prepared ZIF-67/8 and Co₃O₄, ZnO as references, respectively.

(B) The EXAFS spectra of Co, Zn, and Cu K-edge for Zn_{0.2}:Co₁@Cu with Co₃O₄, ZnO, and CuO as references, respectively. See also Figures S15–S18 and Tables S3–S5.

(C) Wavelet transform spectra of Zn foil, ZnO, Zn_{0.2}:Co₁@Cu.

(D) Crystal structure of Zn_{0.2}:Co₁@Cu dodecahedron and magnification of the corner unit that interacted with CO₂.

the curve of ZIF-8. To further investigate the structure, Fourier transforms of Co, Zn, and Cu extended X-ray absorption fine structure (EXAFS) spectra of the Zn_{0.2}:Co₁@Cu catalyst are showed in Figure 4B. It is noted that the second peak of Zn K-edge has a slight shift to 3 Å and a new peak appears around 5 Å compared with ZnO, which suggests a structural distort compared with other catalysts. The Cu K-edge gives rise to a very intense peak at about 2.5 Å, which is similar to the observed peak in the Co K-edge; this means that amounts of Co²⁺ are substituted by Cu²⁺ in the Co₃O₄ structure. As strong evidences, the wavelet transform plots (Figure 4C) show the maximum intensity related to Zn-Zn bonding at ~7 Å⁻¹ in Zn foil and ZnO. The signal of Zn-Zn in Zn_{0.2}:Co₁@Cu shifts to ~6 Å⁻¹, which explains the formation of Zn-Co bond. Besides, the new weak signal at ~8 Å⁻¹ is related to the peak of 5 Å in the Zn EXAFS spectrum; it could be attributed to the nanostructure commutative replacement in the lattices of ZnO and Co₃O₄ phases, which is well consistent with the HRTEM analysis. Hence, it is concluded that some Co²⁺ cations in the tetrahedral units of spinal Co₃O₄ have been successfully replaced by Zn²⁺ and Cu²⁺ in Zn_{0.2}:Co₁@Cu heterojunction. A dodecahedron structure related to the above results and elemental mapping images are illustrated in Figure 4D. In the (100) plane of Zn_{0.2}:Co₁@Cu, five CO₂ molecules could be captured by Co atoms and connected each other in the CO₂ reduction process as well as in plant cell, where the Zn²⁺ and Cu²⁺ dispersed well in samples resulting in a cooperative effect.

Proposed Mechanism of CO₂ Reduction at Zn_x:Co_y@Cu |KHCO₃|BiVO₄

According to the experimental results and characterizations, a possible mechanism for the PEC reduction of CO₂ to paraffin product is proposed and illustrated in Figure 5. Protons could move to the Zn_x:Co_y@Cu photocathode under a low-bias potential and converted to active hydrogen atoms by high-energy photoelectrons in semiconductors. On the other hand, hydroxyl groups (OH⁻) transfer to the photoanode of BiVO₄ releasing O₂ (Seibold and Choi, 2012). When light irradiation is applied to this PEC cell, photogenerated electrons (e⁻) and holes (h⁺) can be generated in Zn_x:Co_y@Cu and quickly separated by the built-in electric field resulting in higher mobilities of charge carriers. Simultaneously, the electrons could be transferred from the conduction band (CB) of Co₃O₄ to the CB of the n-type ZnO and the holes are captured by electrons from the circuit or OH⁻. Hence, the high concentration of photoelectrons was captured by protons in the surfaces to form abundant active hydrogen atoms that could reduce multiple CO₂ molecules into paraffin as the Calvin cycle in plant. In this process, the H₂ release is suppressed due to the rapid rate of CO₂ reduction at multiple active sites of metals and nitrogen.

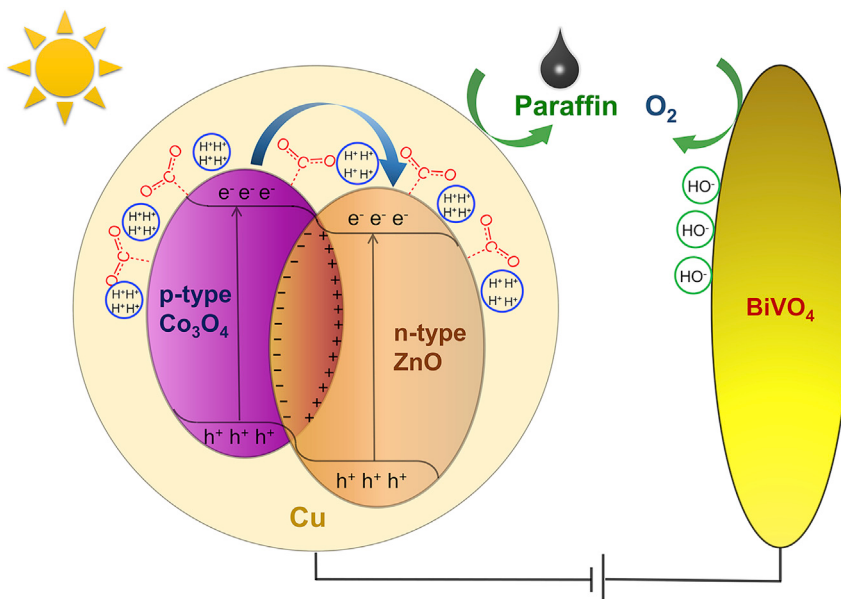


Figure 5. A Proposed Mechanism for the Artificial Photosynthesis of Paraffin

Conclusion

In summary, for the first time we demonstrate a strategy to construct C/N-doped $Zn_x:Co_y@Cu$ heterojunctions as photocathodes, which mimic the Calvin cycle of plants and achieve multiple C-C couplings in our PEC cell to generate the paraffin product. At the optimal photocathode of $Zn_{0.2}:Co_1@Cu$, some Co^{2+} cations in the tetrahedral units of spinal Co_3O_4 have been successfully replaced by Zn^{2+} and Cu^{2+} and form favorable heterojunctions, in which CO_2 molecules are adsorbed and activated by multiple active sites of metals and nitrogen and reduced to paraffin product by active hydrogen atoms. Although there are still many challenges in applying our system to industrial paraffin product, an understanding of the mechanism could provide different perspectives for CO_2 reduction.

Limitations of the Study

- It is very difficult to observe and analyze a specific catalytic reaction with multiple active sites in water.
- The catalytic mechanism of artificial photosynthesis for paraffin could not be verified by theoretical calculations due to the complexity of the catalytic system and multiple coupling of carbon-based species.

METHODS

All methods can be found in the accompanying [Transparent Methods supplemental file](#).

SUPPLEMENTAL INFORMATION

Supplemental Information can be found online at <https://doi.org/10.1016/j.isci.2019.100768>.

ACKNOWLEDGMENTS

This work was financially supported by Natural Science Foundation of Gansu Province, China (17JR5RA212) and the Foundation of State Key Laboratory of Coal Conversion, China (J19-20-913-1). We wish to thank the Electron Microscopy Center of Lanzhou University for the microscopy and microanalysis of our specimens and Institute of High Energy Physics, Chinese Academy of Sciences.

AUTHOR CONTRIBUTIONS

Conceptualization, J.W. and H.J.; Methodology, J.W., Y.G., X.Y., and Y.C.; Investigation, J.W., J.C., Y.W., B.H., and H.J.; Writing – Original Draft, J.W., Y.G., and H.J.; Writing – Review & Editing, J.W., Y.G., and H.J.; Funding Acquisition, H.J.; Supervision, H.J.

DECLARATION OF INTERESTS

The authors declare no competing interests.

Received: July 2, 2019

Revised: November 26, 2019

Accepted: December 9, 2019

Published: January 24, 2020

REFERENCES

- Banerjee, R., Phan, A., Wang, B., Knobler, C., Furukawa, H., Keeffe, M., and Yaghi, O.M. (2008). High-throughput synthesis of zeolitic imidazolate frameworks and application to CO₂ capture. *Science* 319, 939.
- Barton, E.E., Rampulla, D.M., and Bocarsly, A.B. (2008). Selective solar-driven reduction of CO₂ to methanol using a catalyzed p-GaP based photoelectrochemical cell. *J. Am. Chem. Soc.* 130, 6342–6344.
- Bassham, J.A., Benson, A.A., Kay, L.D., Harris, A.Z., Wilson, A.T., and Calvin, M. (1954). The path of carbon in photosynthesis. XXI. The cyclic regeneration of carbon dioxide acceptor. *J. Am. Chem. Soc.* 76, 1760–1770.
- Cardon, F., and Gomes, W.P. (1978). On the determination of the flat-band potential of a semiconductor in contact with a metal or an electrolyte from the Mott-Schottky plot. *J. Phys. D Appl. Phys.* 11, L63–L67.
- Cardoso, J.C., Stulp, S., de Brito, J.F., Flor, J.B.S., Frem, R.C.G., and Zanoni, M.V.B. (2018). MOFs based on ZIF-8 deposited on TiO₂ nanotubes increase the surface adsorption of CO₂ and its photoelectrocatalytic reduction to alcohols in aqueous media. *Appl. Catal. B* 225, 563–573.
- Chang, X., Wang, T., Yang, P., Zhang, G., and Gong, J. (2019). The development of cocatalysts for photoelectrochemical CO₂ reduction. *Adv. Mater.* 31, e1804710.
- Govindjee, and Krogmann, D. (2004). Discoveries in oxygenic photosynthesis (1727–2003): a perspective. *Photosynth. Res.* 80, 15.
- Halmann, M. (1978). Photoelectrochemical reduction of aqueous carbon dioxide on p-type gallium phosphide in liquid junction solar cells. *Nature* 275, 115–116.
- Jia, Y., Xu, Y., Nie, R., Chen, F., Zhu, Z., Wang, J., and Jing, H. (2017). Artificial photosynthesis of methanol from carbon dioxide and water via a Nile red-embedded TiO₂ photocathode. *J. Mater. Chem. A* 5, 5495–5501.
- Lee, S.Y., Jung, H., Kim, N.-K., Oh, H.-S., Min, B.K., and Hwang, Y.J. (2018). Mixed copper states in anodized Cu electrocatalyst for stable and selective ethylene production from CO₂ reduction. *J. Am. Chem. Soc.* 140, 8681–8689.
- Liu, L., Mei, Z., Tang, A., Azarov, A., Kuznetsov, A., Xue, Q.-K., and Du, X. (2016). Oxygen vacancies: the origin of n-type conductivity in ZnO. *Phys. Rev. B* 93, 235305.
- Liu, L., Chen, Z., Wang, J., Zhang, D., Zhu, Y., Ling, S., Huang, K.W., Belmabkhout, Y., Adil, K., Zhang, Y., et al. (2019). Imaging defects and their evolution in a metal-organic framework at sub-unit-cell resolution. *Nat. Chem.* 11, 622–628.
- Loiudice, A., Lobaccaro, P., Kamali, E.A., Thao, T., Huang, B.H., Ager, J.W., and Buonsanti, R. (2016). Tailoring copper nanocrystals towards C2 products in electrochemical CO₂ reduction. *Angew. Chem. Int. Ed.* 55, 5789–5792.
- Long, M., Cai, W., Cai, J., Zhou, B., Chai, X., and Wu, Y. (2006). Efficient photocatalytic degradation of phenol over Co₃O₄/BiVO₄ composite under visible light irradiation. *J. Phys. Chem. B* 110, 20211–20216.
- Lum, Y., and Ager, J.W. (2018). Sequential catalysis controls selectivity in electrochemical CO₂ reduction on Cu. *Energy Environ. Sci.* 11, 2935–2944.
- Luo, W., Wang, J., Zhao, X., Zhao, Z., Li, Z., and Zou, Z. (2013). Formation energy and photoelectrochemical properties of BiVO₄ after doping at Bi³⁺ or V⁵⁺ sites with higher valence metal ions. *Phys. Chem. Chem. Phys.* 15, 1006–1013.
- Mao, J.-H., Perez-Iosada, J., Wu, D., DelRosario, R., Tsunematsu, R., Nakayama, K.I., Brown, K., Bryson, S., and Balmain, A. (2004). Fbxw7/Cdc4 is a p53-dependent, haploinsufficient tumour suppressor gene. *Nature* 432, 775–779.
- Mohamed Reda, G., Fan, H., and Tian, H. (2017). Room-temperature solid state synthesis of Co₃O₄/ZnO p–n heterostructure and its photocatalytic activity. *Adv. Powder Technol.* 28, 953–963.
- Nürnberg, D.J., Morton, J., Santabarbara, S., Telfer, A., Joliot, P., Antonarou, L.A., Ruban, A.V., Cardona, T., Krausz, E., Boussac, A., et al. (2018). Photochemistry beyond the red limit in chlorophyll f-containing photosystems. *Science* 360, 1210–1213.
- Rong, F., Zhao, J., Su, P., Yao, Y., Li, M., Yang, Q., and Li, C. (2015). Zinc–cobalt oxides as efficient water oxidation catalysts: the promotion effect of ZnO. *J. Mater. Chem. A* 3, 4010–4017.
- Schreier, M., Gao, P., Mayer, M.T., Luo, J., Moehl, T., Nazeeruddin, M.K., Tilley, S.D., and Grätzel, M. (2015). Efficient and selective carbon dioxide reduction on low cost protected Cu₂O photocathodes using a molecular catalyst. *Energy Environ Sci* 8, 855–861.
- Seabold, J.A., and Choi, K.-S. (2012). Efficient and stable photo-oxidation of water by a Bismuth Vanadate photoanode coupled with an iron oxyhydroxide oxygen evolution catalyst. *J. Am. Chem. Soc.* 134, 2186–2192.
- Shan, B., Varka, S., Li, T.-T., Trojan-Gautier, L., Brennaman, M.K., Mi, Z., and Meyer, T.J. (2019). Binary molecular-semiconductor p–n junctions for photoelectrocatalytic CO₂ reduction. *Nat. Energy* 4, 290–299.
- Shibata, H., Moulijn, J.A., and Mul, G. (2008). Enabling electrocatalytic Fischer–Tropsch synthesis from carbon dioxide over copper-based electrodes. *Catal. Lett.* 123, 186.
- Tak, Y., and Yong, K. (2008). A novel heterostructure of Co₃O₄/ZnO nanowire array fabricated by photochemical coating method. *J. Phys. Chem. C* 112, 74–79.
- Tang, C., Liu, E., Wan, J., Hu, X., and Fan, J. (2016). Co₃O₄ nanoparticles decorated Ag₃PO₄ tetrapods as an efficient visible-light-driven heterojunction photocatalyst. *Appl. Catal. B* 181, 707–715.
- Wang, Y., He, D., Chen, H., and Wang, D. (2019). Catalysts in electro-, photo- and photocatalytic CO₂ reduction reactions. *J. Photochem. Photobiol. C Photochem. Rev.* 40, 117–149.
- Wu, R., Qian, X., Zhou, K., Wei, J., Lou, J., and Ajayan, P.M. (2014). Porous spinel Zn_xCo_{3-x}O₄ hollow polyhedra templated for high-rate lithium-ion batteries. *ACS Nano* 8, 6297–6303.
- Xu, Y., Wang, S., Yang, J., Han, B., Nie, R., Wang, J., Wang, J., and Jing, H. (2018). In-situ grown nanocrystal TiO₂ on 2D Ti₃C₂ nanosheets for artificial photosynthesis of chemical fuels. *Nano Energy* 51, 442–450.
- Yu, J., Zhuang, S., Xu, X., Zhu, W., Feng, B., and Hu, J. (2015). Photogenerated electron reservoir in hetero-p–n CuO–ZnO nanocomposite device for visible-light-driven photocatalytic reduction of aqueous Cr(VI). *J. Mater. Chem. A* 3, 1199–1207.
- Zhang, Z., Shao, C., Li, X., Wang, C., Zhang, M., and Liu, Y. (2010). Electrospun nanofibers of p-type NiO/n-Type ZnO heterojunctions with enhanced photocatalytic activity. *ACS Appl. Mater. Interfaces* 2, 2915–2923.
- Zhuang, T.-T., Liang, Z.-Q., Seifitokaldani, A., Li, Y., De Luna, P., Burdyny, T., Che, F., Meng, F., Min, Y., Quintero-Bermudez, R., et al. (2018). Steering post-C–C coupling selectivity enables high efficiency electroreduction of carbon dioxide to multi-carbon alcohols. *Nat. Catal.* 1, 421–428.

Supplemental Information

**Photoelectrocatalytic Reduction of CO₂
to Paraffin Using p-n Heterojunctions**

Jinyuan Wang, Yongji Guan, Xiaogang Yu, Youzhi Cao, Jiazang Chen, Yilin Wang, Bin Hu, and Huanwang Jing

Supplemental Information

Supplemental Figures and Tables

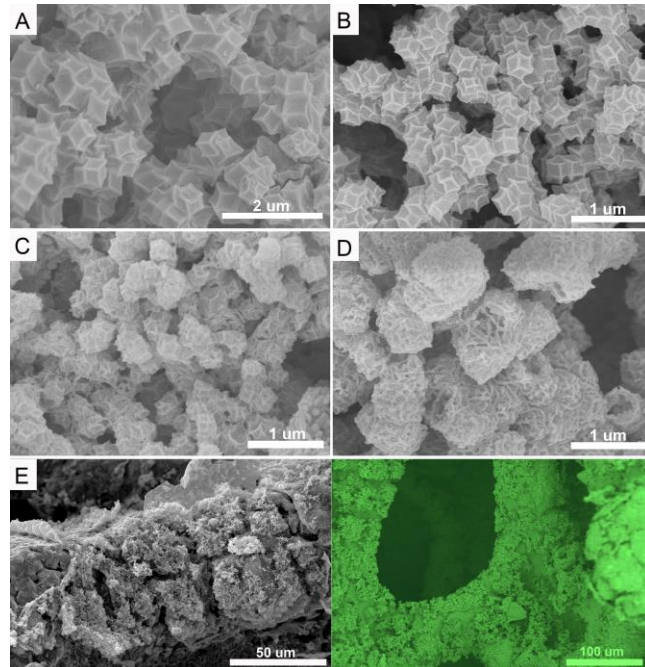


Figure S1. SEM images of $Z_{nx}:C_{oy}@\text{Cu}$. **A**, $Z_{n0}:C_{o1}@\text{Cu}$, **B**, $Z_{n0.2}:C_{o1}@\text{Cu}$, **C**, $Z_{n1}:C_{o1}@\text{Cu}$, **D**, $Z_{n1}:C_{o0}@\text{Cu}$ and **E**, large thumbnails of $Z_{n0.2}:C_{o1}@\text{Cu}$. Related to Figure 1.

The SEM image of the $Z_{nx}:C_{oy}@\text{Cu}$ suggested that the diameters of $Z_{n0}:C_{o1}@\text{Cu}$ and $Z_{n1}:C_{o0}@\text{Cu}$ are nearly 1 μm. The volume of bimetallic $Z_{nx}:C_{oy}@\text{Cu}$ is relatively small, the diameter of $Z_{n0.2}:C_{o1}@\text{Cu}$ and $Z_{n1}:C_{o1}@\text{Cu}$ are about 500 nm. As the proportion of Zn in the bimetallic $Z_{nx}:C_{oy}@\text{Cu}$ increases, it changes from a regular polyhedron to a surface-porous irregular particle. The zeolitic imidazolate frameworks (ZIFs) is uniformly loaded on the Cu foam.

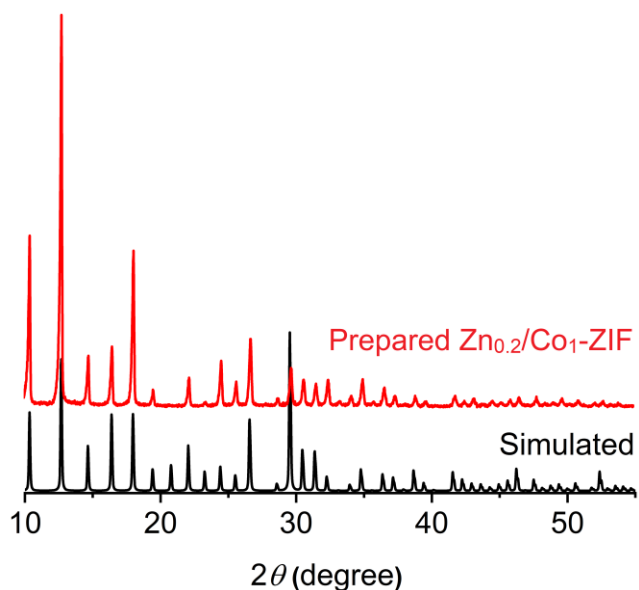


Figure S2. The XRD patterns of as-prepared $Z_{n0.2}/C_{o1}-\text{ZIFs}$ sample. Related to Figure 1.

The prepared XRD pattern matches well with the simulated one which is corresponding to a sodalite structure of pure cubic ZIF-8 as literature reported(Fairen-Jimenez et al., 2011; Qin et al., 2017). The sharp and strong characteristic peaks reflect the high crystallinity of the material prepared with the synthesizing protocol.

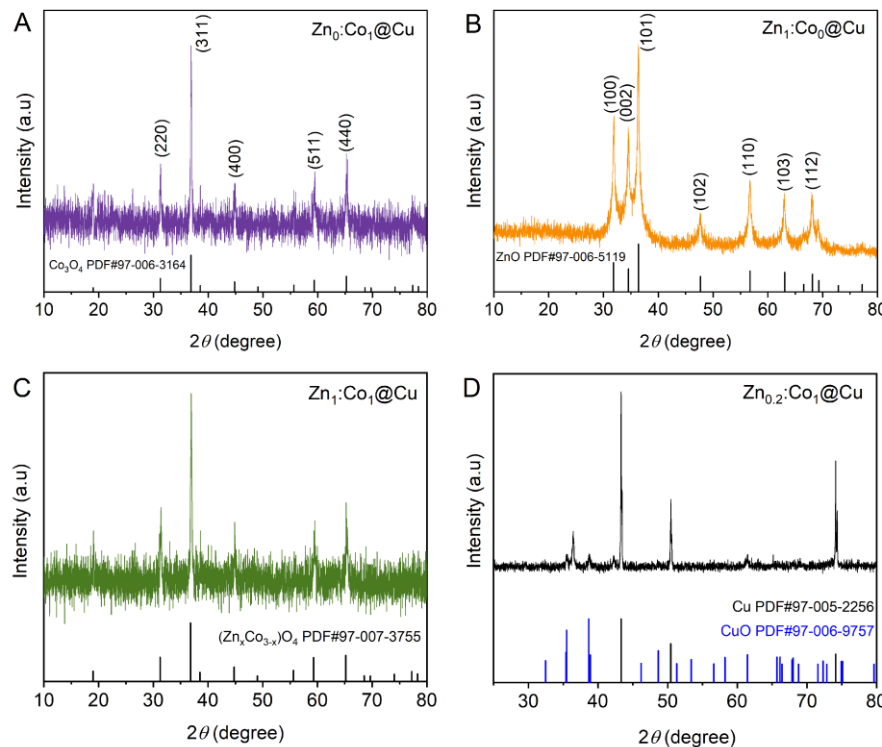


Figure S3. XRD patterns of **A**, $Zn_0:Co_1$, **B**, $Zn_1:Co_0$, **C**, $Zn_1:Co_1$ and **D** $Zn_{0.2}:Co_1@Cu$. Related to Figure 1.

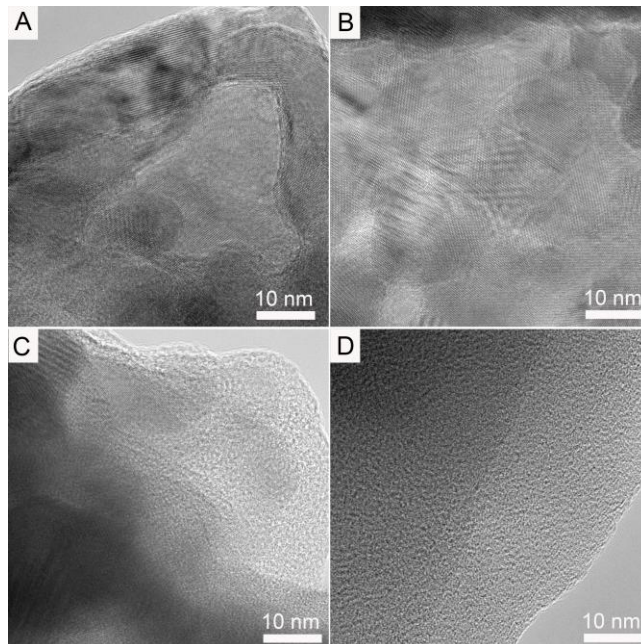


Figure S4. HRTEM images of **A**, $Zn_0:Co_1@Cu$, **B**, $Zn_{0.2}:Co_1@Cu$, **C**, $Zn_1:Co_1@Cu$ and **D** $Zn_1:Co_0@Cu$. Related to Figure 1.

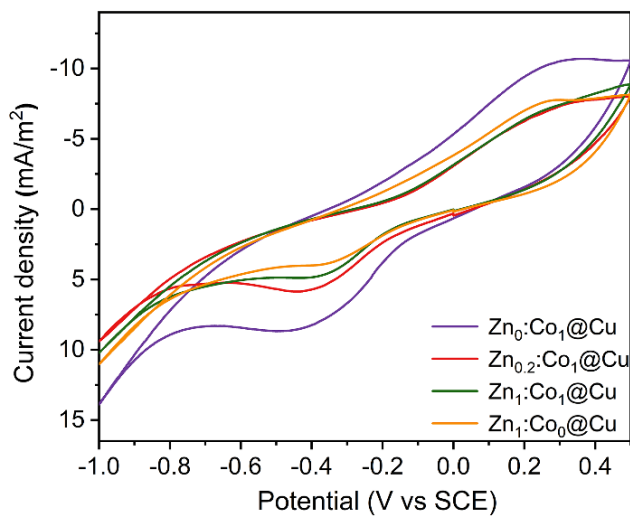


Figure S5. CV curves of $Z_{nx}:C_{oy}@\text{Cu}$ in PEC condition. Related to Figure 2 and Figure S6.

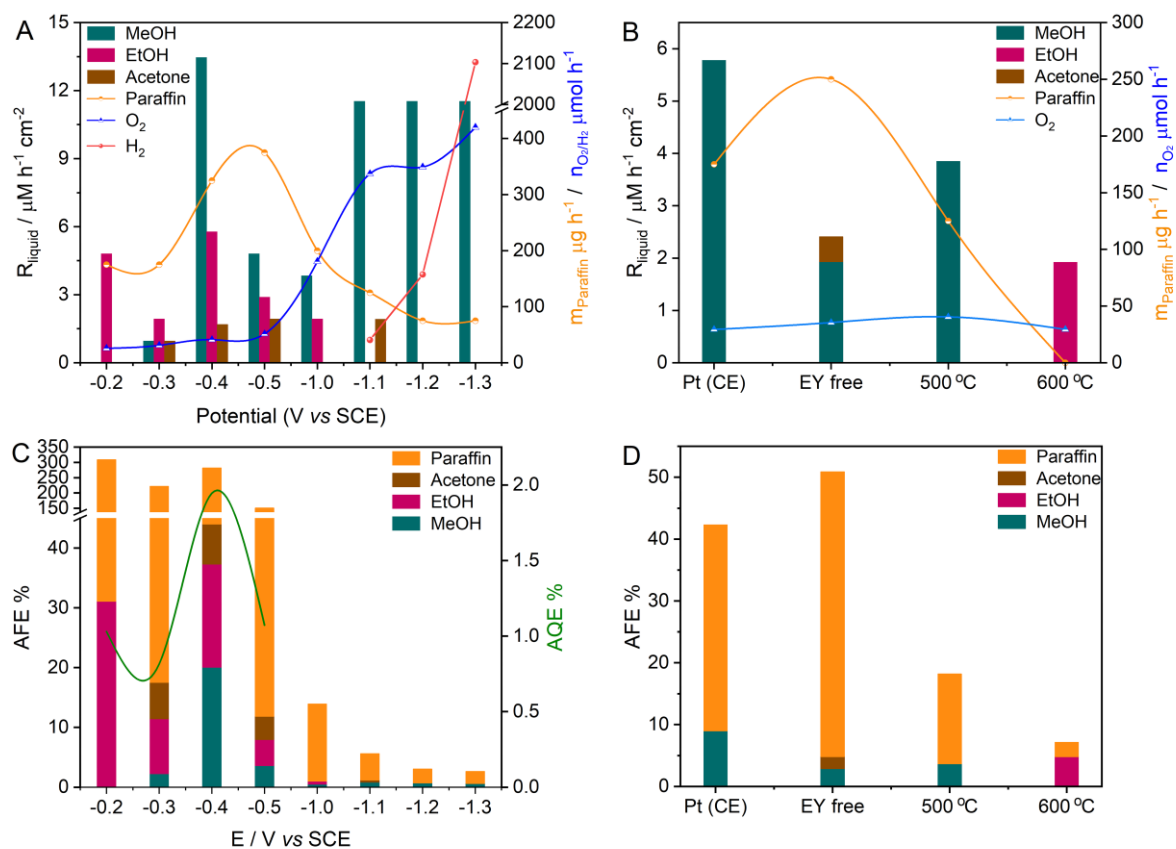


Figure S6. Comparison of catalytic performance. **A, C**, rate and efficiency (AQE, AFE) of the PEC activities of $Z_{n0.2}:C_{o1}@\text{Cu}$ at different potential. **B, D**, rate and efficiency under the follow condition: Pt foil as a photoanode; the electrolyte do not contain EY; as well as pyrolysis $Z_{n0.2}/C_{o1}$ -ZIFs under 500°C and 600°C, respectively. The AQE is not calculated in the case of the AFE is less than 100%. Related to Figure 2 and Figure S5.

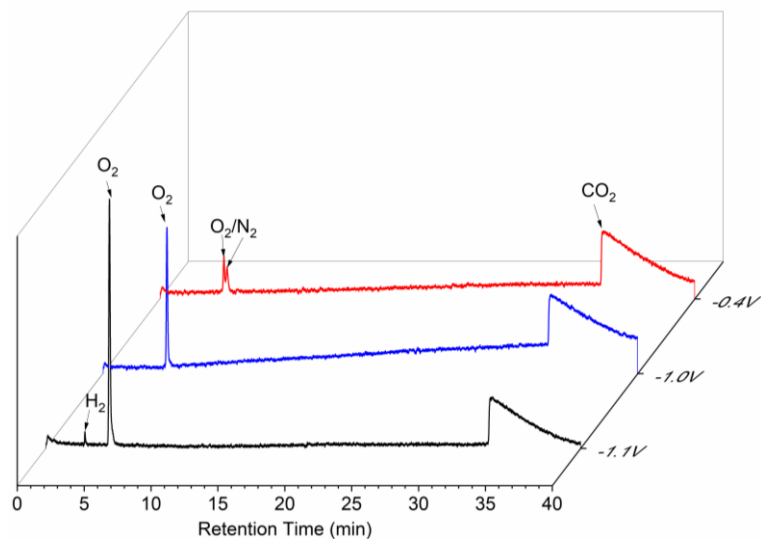


Figure S7. Representative GC data showing the signal of H₂ appeared under -1.1V vs. SCE. Related to Figure 2 and Figure S6.

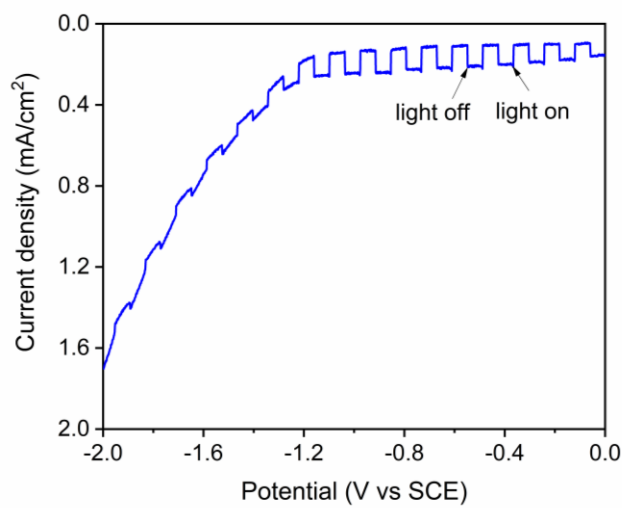


Figure S8. Photocurrent densities by solar irradiation of Zn_{0.2}:Co₁@Cu | KHCO₃ | BiVO₄ under the PEC condition with chopped light. Related to Figure 2.

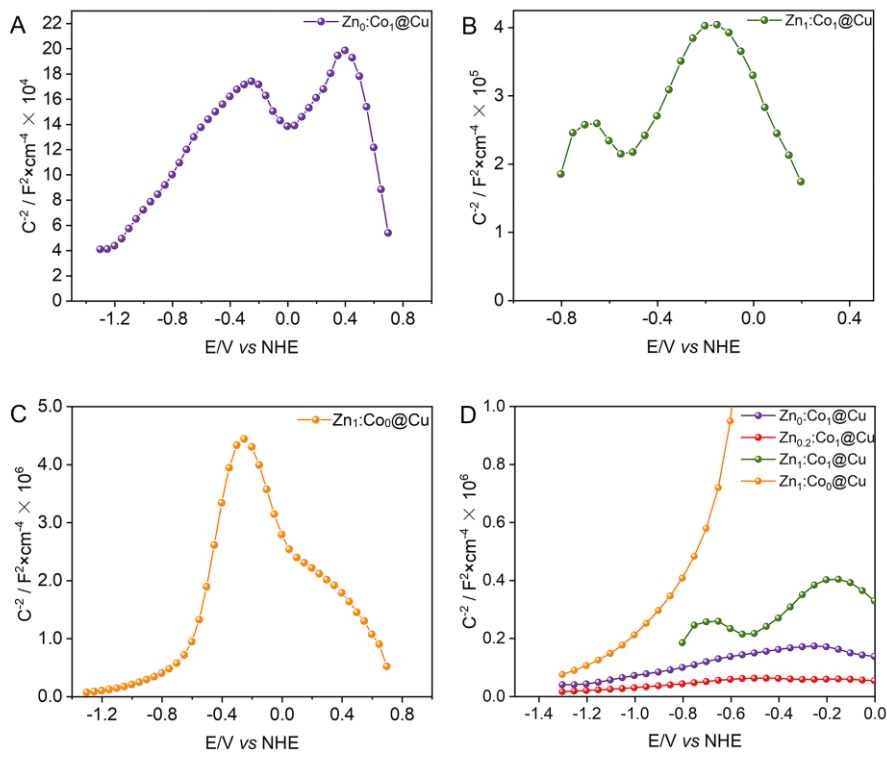


Figure S9. M-S plots of Zn_x:Co_y@Cu electrode. M-S analysis is carried out with Zn_x:Co_y@Cu work electrodes, Pt foil counter electrode and reference electrode Ag/AgCl (Sat. KCl). The electrolyte contains 0.1 M KHCO₃ solution and non-CO₂ bubble. After that, M-S plots are generated based on capacitance that is derived from the electrochemical impedance obtained at each potential with the frequency of 0.5 kHz under dark. Related to Figure 2.

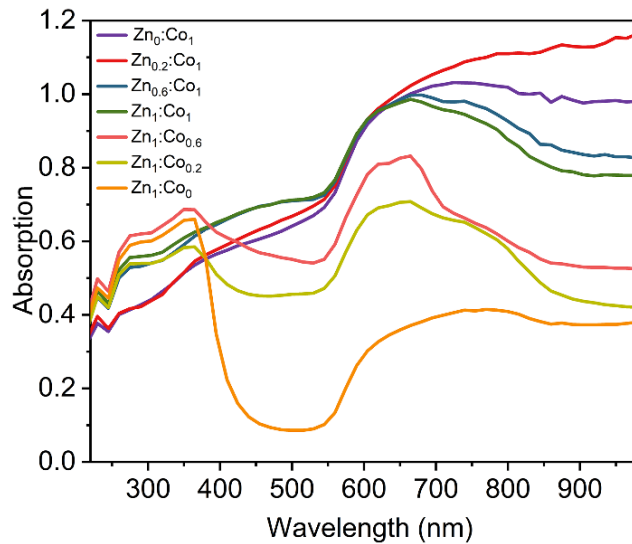


Figure S10. The solid-state UV-vis absorption spectra of the photocathodes Zn_x:Co_y@Cu. Related to Figure 2.

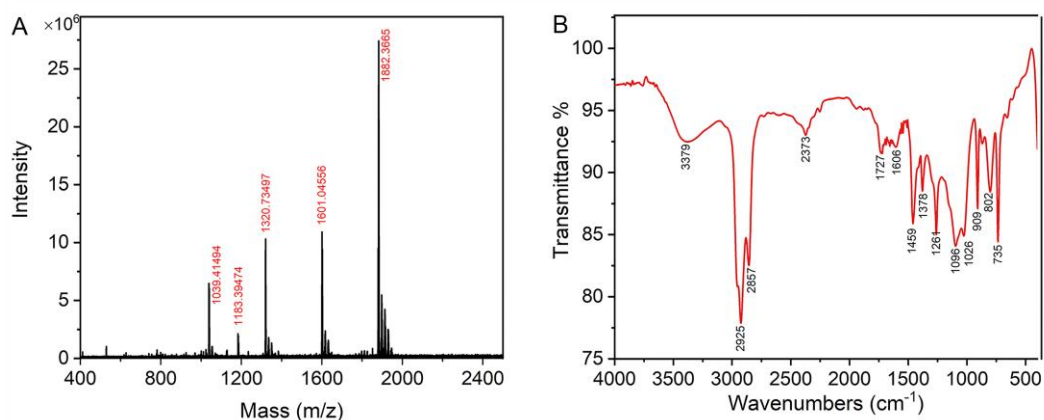


Figure S11. Comparison for paraffin products using $^{12}\text{CO}_2$ as raw materials. **A**, MALDI-TOF MS analysis about paraffin which is obtained after reaction of 4h under -0.4V versus SCE using $\text{Zn}_{0.2}\text{:Co}_1\text{@Cu}$ as photocathode. **B**, the corresponding infrared (IR) spectroscopy analysis. Related to Figure 3 and Figure S12.

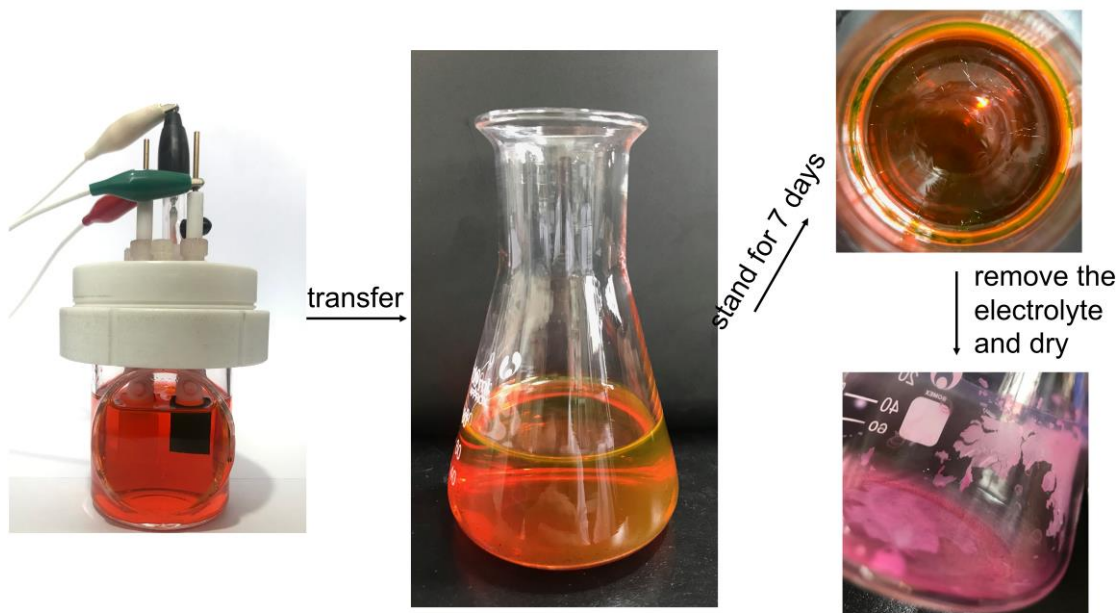


Figure S12. Paraffin product photos. Related to Figure 3 and Figure S11.

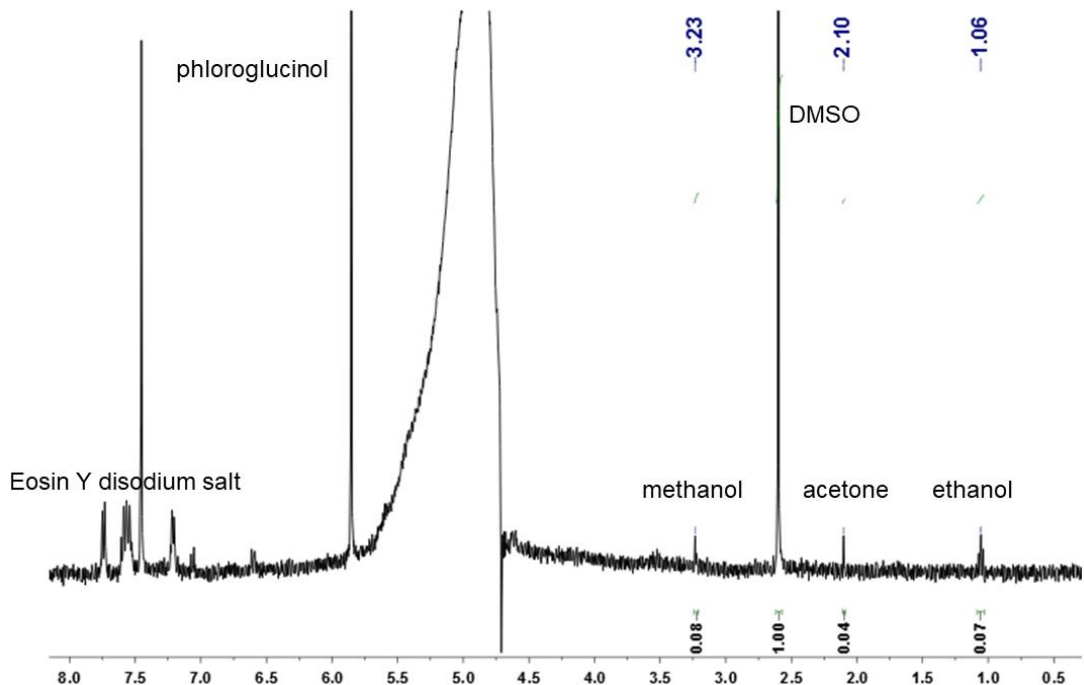


Figure S13. Representative NMR spectrum showing the signals of the liquid product of PEC CO₂ reduction: methanol, ethanol, acetone, Eosin Y disodium salt, and the internal standard of DMSO and phloroglucinol. The concentration of methanol, ethanol and acetone was calculated based on the ratio of the integrals of formate to DMSO. Related to Figure 2, Figure S6 and Figure S7.

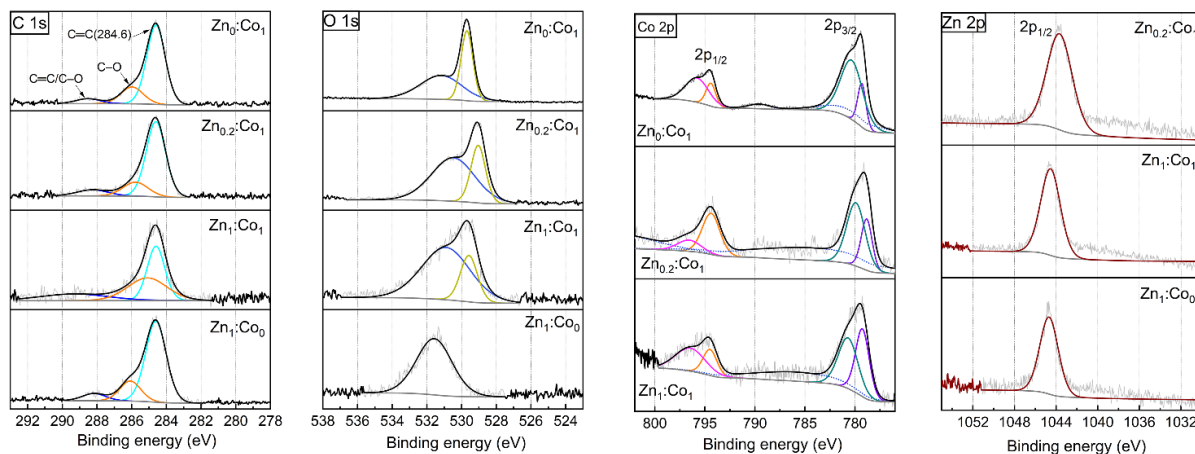


Figure S14. X-ray photoelectron spectroscopy of Znx:Coy@Cu. The chemical bonding energy of C 1s, O 1s, Co 2p and Zn 2p for Znx:Coy@Cu. Compared to Zn₀:Co₁@Cu, a negative shift is observed in Zn_{0.2}:Co₁@Cu sample for Co 2p_{3/2}. Similarly, a negative shift is observed in Zn_{0.2}:Co₁@Cu for Zn 2p_{1/2} compared with Zn₁:Co₀@Cu. The explanation of the shift is probably due to the incorporation of Zn²⁺ into Co₃O₄. Related to Figure 4.

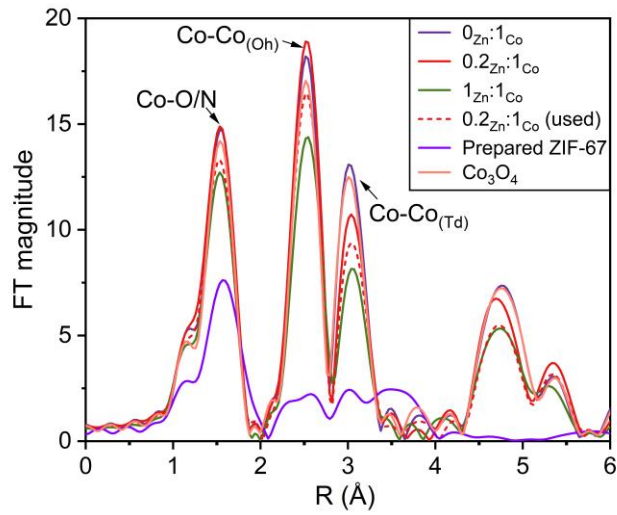


Figure S15. The EXAFS spectra of Co K-edge for $\text{Zn}_x:\text{Co}_y@\text{Cu}$, Co_3O_4 and prepared ZIF-67, respectively. Related to Figure 4.

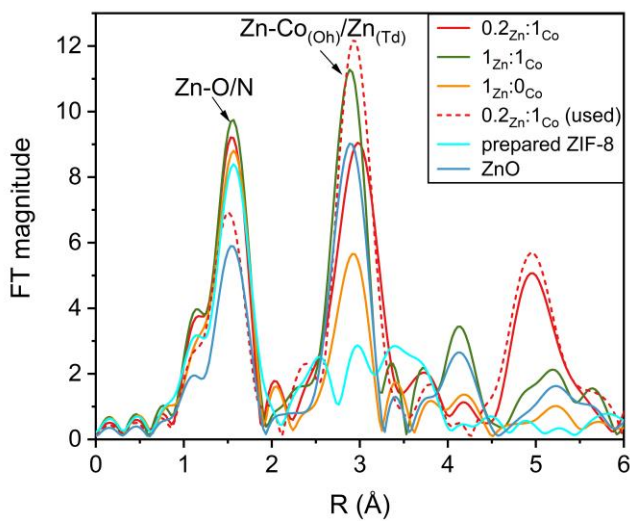


Figure S16. The EXAFS spectra of Zn K-edge for $\text{Zn}_x:\text{Co}_y@\text{Cu}$, ZnO and prepared ZIF-8, respectively. Related to Figure 4.

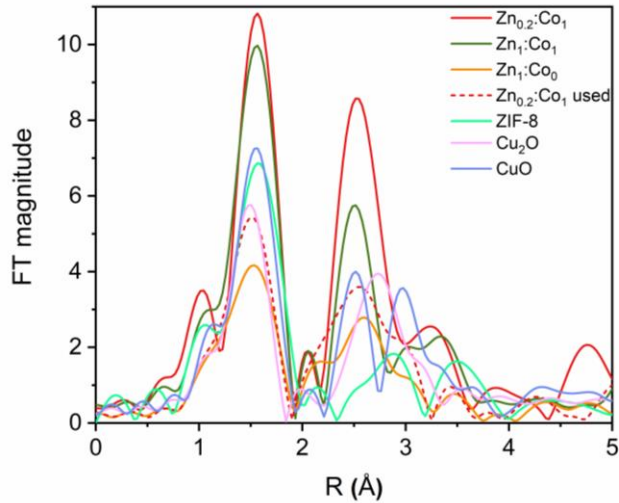


Figure S17. The EXAFS spectra of Cu K-edge for $Zn_x:Co_y@Cu$, CuO and CuO_2 , respectively. Related to Figure 4.

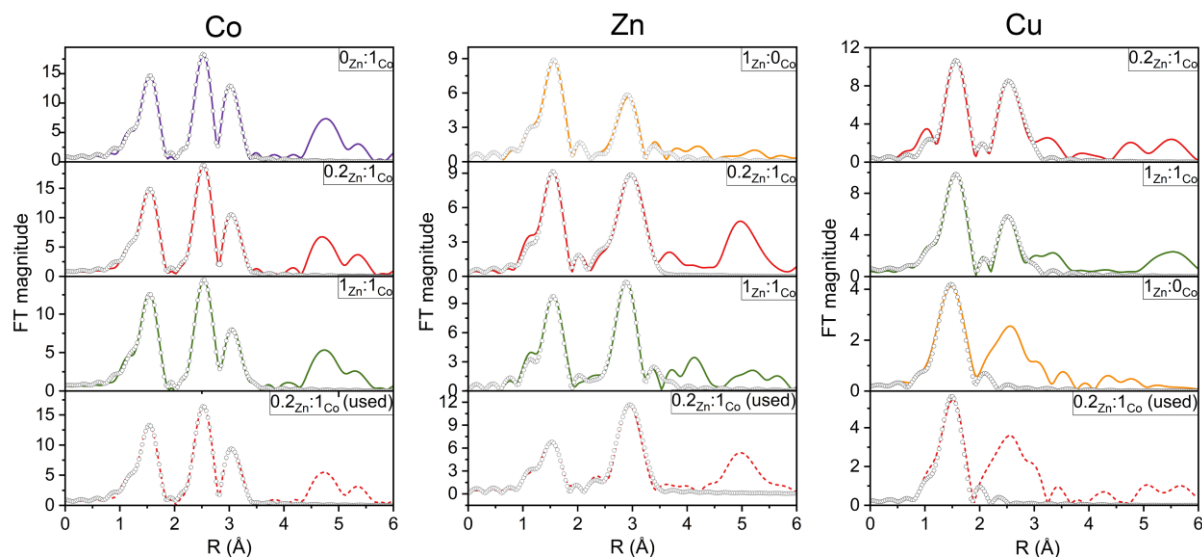


Figure S18. EXAFS fitting curve for $Zn_x:Co_1@Cu$. Related to Figure 4.

Table S1. Elemental analysis using ICP-OES for Co, Zn and Cu with different samples (mass%). The data are average value of three times. Related to Figure 1.

| Sample | Co(%) | Zn(%) | Cu(%) |
|-----------------|-------|-------|--------|
| $Zn_0:Co_1$ | 78.47 | 0 | 1.442 |
| $Zn_{0.2}:Co_1$ | 48.61 | 17.79 | 10.295 |
| $Zn_1:Co_1$ | 24.07 | 55.80 | 1.709 |
| $Zn_1:Co_0$ | 0 | 65.65 | 0.753 |

Table S2. BET surface areas and pore volumes of the samples. BET surface area calculations were based on the adsorption isotherms using P/P_0 from 0.005 to 0.1. Related to Figure 1.

| Sample | S_{BET} (m^2/g) ^a | V_{total} (cm^3/g) | V_{mic} (cm^3/g) | Aperture |
|------------------------------------|---|---|---|----------|
| Zn ₀ :Co ₁ | 7.5060 | 0.0376 | 0.0022 | 31.7002 |
| Zn _{0.2} :Co ₁ | 15.4993 | 0.0819 | 0.0016 | 28.1005 |
| Zn ₁ :Co ₁ | 7.8388 | 0.0280 | 0.0024 | 36.6862 |
| Zn ₁ :Co ₀ | 12.5728 | 0.0279 | 0.0030 | 19.1169 |

Table S3. EXAFS fitting parameters at the Co K-edge for various sample. ^a N : correction. R factor: goodness of fit. S_0^2 , 0.77, was obtained from the experimental EXAFS fit of Co₃O₄ reference by fixing CN as the known crystallographic value and was fixed to all the samples. Related to Figure 4.

| Sample | Shell | N ^a | R (\AA) ^b | σ^2 ($\text{\AA}^2 \cdot 10^3$) ^c | ΔE^0 (eV) ^d | R factor (%) |
|--|-------|------------------|-----------------------------------|---|--------------------------------|----------------|
| Zn ₀ :Co ₁ | Co-O | 5.6 | 1.92 | 3.2 | 5.4 | 0.2 |
| | Co-Co | 4.4 | 2.86 | 3.3 | 4.4 | |
| | Co-Co | 10.4 | 3.37 | 7.1 | 1.9 | |
| Zn _{0.2} :Co ₁ | Co-O | 6.1 | 1.92 | 3.6 | 5.1 | 0.2 |
| | Co-Co | 5.5 | 2.86 | 4.1 | 3.6 | |
| | Co-Co | 7.7 | 3.37 | 6.5 | 3.9 | |
| Zn ₁ :Co ₁ | Co-O | 5.5 | 1.92 | 4.0 | 4.4 | 0.3 |
| | Co-Co | 3.8 | 2.86 | 3.8 | 3.4 | |
| | Co-Co | 9.7 | 3.37 | 10.4 | 6.4 | |
| Zn _{0.2} :Co ₁ (used) | Co-O | 5.5 | 1.91 | 3.6 | 4.4 | 0.3 |
| | Co-Co | 4.9 | 2.86 | 4.2 | 3.6 | |
| | Co-Co | 6.8 | 3.37 | 6.5 | 3.6 | |

Table S4. EXAFS fitting parameters at the Cu K-edge for various samples. ^a N: coordination numbers; ^b R: bond distance; ^c σ^2 : Debye-Waller factors; ^d ΔE_0 : the inner potential correction. R factor: goodness of fit. S_0^2 , 0.75, was obtained from the experimental EXAFS fit of CuO reference by fixing CN as the known crystallographic value and was fixed to all the samples. Related to Figure 4.

| Sample | Shell | N ^a | R (Å) ^b | σ^2 (Å ² ·10 ³) ^c | ΔE^0 (eV) ^d | R factor (%) |
|---|-------|----------------|--------------------|--|--------------------------------|--------------|
| Zn ₁ :Co ₀ | Cu-O | 2.1 | 1.89 | 6.1 | 8.9 | 0.7 |
| Zn _{0.2} :Co ₁ | Cu-O | 4.1 | 1.95 | 2.1 | 6.4 | 2.0 |
| | Cu-Cu | 4.7 | 2.89 | 6.5 | 3.2 | |
| Zn ₁ :Co ₁ | Cu-O | 5.4 | 1.96 | 5.7 | 7.3 | 1.0 |
| | Cu-Cu | 2.2 | 2.86 | 4.5 | -2.0 | |
| Zn _{0.2} :Co ₁ (used) | Cu-O | 2.4 | 1.89 | 4.8 | 7.5 | 1.6 |
| CuO | Cu-O | 4 | 1.94 | 4.9 | 7.2 | 0.3 |

Table S5. EXAFS fitting parameters at the Zn K-edge for various samples. ^a N: coordination numbers; ^b R: bond distance; ^c σ^2 : Debye-Waller factors; ^d ΔE_0 : the inner potential correction. R factor: goodness of fit. S_0^2 , 0.77, was obtained from the experimental EXAFS fit of ZnO reference by fixing CN as the known crystallographic value and was fixed to all the samples. Related to Figure 4.

| Sample | Shell | N ^a | R (Å) ^b | σ^2 (Å ² ·10 ³) ^c | ΔE_0 (eV) ^d | R factor (%) |
|---|-------|----------------|--------------------|--|--------------------------------|--------------|
| Zn ₁ :Co ₀ | Zn-O | 0.9 | 1.86 | 1.3 | 3.9 | 0.8 |
| | Zn-O | 2.7 | 1.98 | 1.0 | | |
| | Zn-Zn | 3.4 | 3.23 | 8.0 | 4.9 | |
| Zn _{0.2} :Co ₁ | | | | | | 2.0 |
| | Zn-O | 3.7 | 1.96 | 3.5 | 3.7 | |
| | Zn-Zn | 19.2 | 3.33 | 17.0 | -4.7 | |
| Zn ₁ :Co ₁ | Zn-O | | | | | 1.1 |
| | Zn-O | 4.0 | 1.97 | 3.9 | 4.6 | |
| | Zn-Zn | 10.6 | 3.22 | 11.0 | 2.5 | |
| Zn _{0.2} :Co ₁ (used) | Zn-O | | | | | 4.0 |
| | Zn-O | 4.5 | 1.96 | 8.2 | -0.5 | |
| | Zn-Zn | 10.0 | 3.32 | 9.0 | -8.2 | |
| ZnO | Zn-O | 1 | 1.88 | 0.2 | 5.5 | 0.5 |
| | Zn-O | 3 | 1.99 | 0.9 | | |
| | Zn-Zn | 12 | 3.22 | 9.6 | 2.9 | |

The acquired EXAFS data were processed according to the standard procedures using the ATHENA module implemented in the IFEFFIT software packages. The k³-weighted EXAFS spectra were obtained by subtracting the post-edge background from the overall absorption and then normalizing with respect to the edge-jump step. Subsequently, k³-weighted $\chi(k)$ data of K-edge were Fourier transformed to real (R) space using a hanning windows ($dk=1.0 \text{ \AA}^{-1}$) to separate the EXAFS contributions from different coordination shells. To obtain the quantitative structural parameters around central atoms, least-squares curve parameter fitting was performed using the ARTEMIS module of IFEFFIT software packages.

Transparent Methods

Chemicals and materials.

Carbon dioxide (CO_2) gas was purchased as 99.999% purity. $^{13}\text{CO}_2$ was obtained from Aldrich Company. Tetrabromofluorescein, DMSO, phloroglucinol, Eosin Y disodium salt, potassium bicarbonate, 2-Methylimidazole, Zinc (II) nitrate hexahydrate ($\text{Zn}(\text{NO}_3)_2 \cdot 6\text{H}_2\text{O}$) and Cobalt(II) nitrate hexahydrate ($\text{Co}(\text{NO}_3)_2 \cdot 6\text{H}_2\text{O}$) were ordered from Sinopharm Chemical Reagent Co., Ltd. D_2O were purchased from Cambridge Isotope Laboratories, Inc. Other chemicals and reagents were purchased from Adamas-beta[®] as analytical grade commercial products and used for reaction without further purification unless otherwise indication.

Characterization.

X-ray diffraction (XRD) patterns of materials were recorded on an X'Pert PRO diffractometer. Scanning electron microscope (SEM) was performed on Apreo S. Transmission electron microscopy (TEM) and corresponding energy dispense spectroscopy (EDS) mapping were performed on FEI Talos F200s under accelerating voltage of 200 KV. X-ray photoelectron spectroscopy (XPS) of samples were measured using a VG Scientific ESCALB210-XPS photoelectron spectrometer equipped with an Mg K α X-ray resource. For the core-level spectra, the carbon 1s feature located at 284.6.0 eV was used to calibrate the binding energies. Elemental analysis of metal quantity was detected by ICP-OES (PQ 9000). The Fourier transform infrared spectroscopy (FTIR) were recorded with KBr pellets in the range of 4000-400 cm^{-1} on a NEXUS 670 spectrometer. The optical absorption properties of electrodes were characterized by a UV-vis spectrophotometer (UV-2600, Shimadzu).

^1H and ^{13}C NMR spectra were recorded on a Varian AM-400 spectrometer using D_2O , DMSO and phloroglucinol as an internal standard. Gas chromatograph (GC) analyses of gaseous product were carried out on a Varian CP-3800 GC equipped with flame ionization detector (FID) and thermal conductivity detector (TCD) detectors. A solar simulator PLS-SXE300C was used as light source. A CHI660E electrochemical workstation was used for different parameters of experiments. A standard Si-solar cell of Fraunhofer ISE was used to calibrate the light density of solar simulator.

Preparation of $\text{Zn}_x:\text{Co}_y\text{-ZIF@Cu}$.

A series of samples are prepared with different Zn to Co molar ratios, which grow in situ on Cu foam and record as $\text{Zn}_x:\text{Co}_y\text{-ZIF@Cu}$, where x/y is the molar ratio of $\text{Zn}(\text{NO}_3)_2 \cdot 6\text{H}_2\text{O}$ to $\text{Co}(\text{NO}_3)_2 \cdot 6\text{H}_2\text{O}$ and their total moles are 3 mmol. All the photocathodes of $\text{Zn}_x:\text{Co}_y\text{-ZIF@Cu}$ are prepared in the same method, and the preparation of $\text{Zn}_{0.2}\text{Co}_1\text{-ZIFs@Cu}$ is described in detail as following. The Cu foam is cut into a square electrode ($1.5 \times 2 \text{ cm}$), then is successively washed with isopropanol, ethanol, acetone, hydrochloric acid and deionized H_2O under ultrasonication for 30 min and natural drying before use. In a typical synthesis process, $\text{Co}(\text{NO}_3)_2 \cdot 6\text{H}_2\text{O}$ (148.5 mg, 0.5 mmol) and $\text{Zn}(\text{NO}_3)_2 \cdot 6\text{H}_2\text{O}$ (727.5 mg, 2.5 mmol) are dissolved in 30 ml methanol (MeOH) to form a clear solution. Then the Cu foam is soaked in above solution and 10 mL MeOH containing 2-methylimidazole (984 mmg, 12 mmol) is subsequently droped in 10 minutes. The reaction is incubated at room temperature for 24 h with slow stirring. The synthesized $\text{Zn}_{0.2}\text{Co}_1\text{-ZIF@Cu}$ is washed with ethanol for several times and goes through natural drying overnight. The other mole ratio of $\text{Zn}_x:\text{Co}_y\text{-ZIF@Cu}$ have prepared with the same process as mentioned above.

Preparation of $\text{Zn}_x:\text{Co}_y\text{@Cu}$.

The $\text{Zn}_x:\text{Co}_y\text{@Cu}$ are placed in a tube furnace and then heat up to 400 °C for 30 min with a ramp of 5 °C min^{-1} under argon gas flow. After that, the argon gas is switched off, and the furnace is still kept in air at this temperature for another 30 min. Thus, the photocathode materials of $\text{Zn}_x:\text{Co}_y\text{@Cu}$ are prepared.

Photoelectrochemical measurement.

Photoelectrochemical measurements are carried out with a CHI660E electrochemical workstation in actual three-

electrode PEC reaction condition in order to detect the state of the real reaction. The electrochemical impedance spectroscopy (EIS) experiments are conducted with amplitude of 10 mV and frequency ranging from 0.001 Hz to 1 MHz in 0.1 M KHCO₃ solution (CO₂ saturation). E/V vs. RHE = E (vs. Hg/HgCl₂) + 0.242V + 0.0591 × pH (6.8).

PEC activity measurement.

The PEC experiments are carried out in a PEC cell of Zn_x:Co_y@Cu|KHCO₃|BiVO₄ using SCE as reference electrode. The above PEC cell contains KHCO₃ aqueous solution (0.1 M; 80 mL) with or without Eosin Y disodium salt (0.01 M) as sensitizer and then the solution is saturated with a stream of high purity CO₂ for 30 min (pH = 6.8). After that, the PEC experiment is conducted under irradiation of simulated sunlight (AM 1.5G (Perfectlight), 200 mW cm⁻²) with different potential. The liquid products are quantified by NMR spectroscopy and the ¹H spectrum are measured with H₂O suppression using a pre-saturation method, in which appropriate electrolyte is mixed with 35 μL standard liquid (1 mL D₂O + 7 mM dimethyl sulfoxide + 36 mM phloroglucinol). The gas products are analyzed using gas chromatograph (GC). The paraffin products are detected with MALDI-TOF MS.

Rate and apparent quantum efficiency (AQE) measurement.

The rate and efficiency (AQE and AFE) are measured under the ordinary PEC reaction condition and calculated according to the following equation,

$$\text{Rate (liquid product)} = \frac{C_{\text{DMSO}}(\mu\text{M}) \times \text{Relative Area}_{\text{product}}}{\text{Time(h)} \times 1.82(\text{cm}^{-2})}$$

$$\text{AFE (\%)} = \frac{\sum (\text{moles product} \times \text{electron transfer number(n)})}{\text{moles of electrons counted}}$$

$$\text{AQE (\%)} = \frac{\sum (\text{moles product} \times n) - \text{moles of electrons counted}}{\text{moles of photons irradiated on electrode}}$$

The moles of photons irradiated on electrode

$$= \frac{\text{light density(mW cm}^{-2}\text{)} \times \text{suface area(cm}^2\text{)} \times \text{radiation time(s)}}{\text{photon (500 nm) energy(J)} \times 6.02 \times 10^{23}}$$

XAFS measurements.

The X-ray absorption fine structure spectra (XAFS) are collected at 1W1B station in Beijing Synchrotron Radiation Facility (BSRF). The storage rings of BSRF is operated at 2.5 GeV with a maximum current of 250 mA. Using Si (111) double-crystal monochromator, the data collection is carried out in transmission mode using ionization chamber. All spectra are collected in ambient condition.

Supplementary References

- Fairen-Jimenez, D., Moggach, S.A., Wharmby, M.T., Wright, P.A., Parsons, S., and Düren, T. (2011). Opening the Gate: Framework Flexibility in ZIF-8 Explored by Experiments and Simulations. *J Am Chem Soc* *133*, 8900-8902.
- Qin, J., Wang, S., and Wang, X. (2017). Visible-light reduction CO₂ with dodecahedral zeolitic imidazolate framework ZIF-67 as an efficient co-catalyst. *Appl Catal B* *209*, 476-482.